

# Tunable beam steering enabled by graphene metamaterials

B. Orazbayev,<sup>1</sup> M. Beruete,<sup>1,2,\*</sup> and I. Khromova<sup>1,3,4</sup>

<sup>1</sup>Antennas Group-TERALAB, Universidad Pública de Navarra, Pamplona 31006, Spain

<sup>2</sup>Institute of Smart Cities, Public University of Navarra, 31006 Pamplona, Spain

<sup>3</sup>Department of Physics, King's College London, Strand, London WC2R 2LS, UK

<sup>4</sup>The International Research Centre for Nanophotonics and Metamaterials, ITMO University, Birjevaya line V.O. 14, St. Petersburg 199034, Russia

\*miguel.beruete@unavarra.es

**Abstract:** We demonstrate tunable mid-infrared (MIR) beam steering devices based on multilayer graphene-dielectric metamaterials. The effective refractive index of such metamaterials can be manipulated by changing the chemical potential of each graphene layer. This can arbitrarily tailor the spatial distribution of the phase of the transmitted beam, providing mechanisms for active beam steering. Three different beam steerer (BS) designs are discussed: a graded-index (GRIN) graphene-based metamaterial block, an array of metallic waveguides filled with graphene-dielectric metamaterial and an array of planar waveguides created in a graphene-dielectric metamaterial block with a specific spatial profile of graphene sheets doping. The performances of the BSs are numerically analyzed, showing the tunability of the proposed designs for a wide range of output angles (up to approximately 70°). The proposed graphene-based tunable beam steering can be used in tunable transmitter/receiver modules for infrared imaging and sensing.

©2016 Optical Society of America

**OCIS codes:** (160.3918) Metamaterials; (230.7370) Waveguides; (160.4236) Nanomaterials; (260.3060) Infrared.

---

## References and links

1. W. Li, B. Chen, C. Meng, W. Fang, Y. Xiao, X. Li, Z. Hu, Y. Xu, L. Tong, H. Wang, W. Liu, J. Bao, and Y. R. Shen, "Ultrafast all-optical graphene modulator," *Nano Lett.* **14**(2), 955–959 (2014).
2. A. Fallahi and J. Perruisseau-Carrier, "Design of tunable bi-periodic graphene metasurfaces," *Phys. Rev. B* **86**(19), 195408 (2012).
3. L. Ju, B. Geng, J. Horng, C. Girit, M. Martin, Z. Hao, H. A. Bechtel, X. Liang, A. Zettl, Y. R. Shen, and F. Wang, "Graphene plasmonics for tunable terahertz metamaterials," *Nat. Nanotechnol.* **6**(10), 630–634 (2011).
4. A. Vakil and N. Engheta, "Transformation optics using graphene," *Science* **332**(6035), 1291–1294 (2011).
5. J. T. Kim and S.-Y. Choi, "Graphene-based plasmonic waveguides for photonic integrated circuits," *Opt. Express* **19**(24), 24557–24562 (2011).
6. X. Zhu, W. Yan, N. A. Mortensen, and S. Xiao, "Bends and splitters in graphene nanoribbon waveguides," *Opt. Express* **21**(3), 3486–3491 (2013).
7. Y. Dai, X. Zhu, N. A. Mortensen, J. Zi, and S. Xiao, "Nanofocusing in a tapered graphene plasmonic waveguide," *J. Opt.* **17**(6), 065002 (2015).
8. S. He, X. Zhang, and Y. He, "Graphene nano-ribbon waveguides of record-small mode area and ultra-high effective refractive indices for future VLSI," *Opt. Express* **21**(25), 30664–30673 (2013).
9. J. Lao, J. Tao, Q. J. Wang, and X. G. Huang, "Tunable graphene-based plasmonic waveguides: nano modulators and nano attenuators," *Laser Photonics Rev.* **8**(4), 569–574 (2014).
10. O. Sydoruk, E. Tatartschuk, E. Shamonina, and L. Solymar, "Analytical formulation for the resonant frequency of split rings," *J. Appl. Phys.* **105**(1), 014903 (2009).
11. R. Marqués, F. Martín, and M. Sorolla, *Metamaterials with Negative Parameters: Theory, Design, and Microwave Applications* (John Wiley & Sons, 2008).
12. D. Rainwater, A. Kerkhoff, K. Melin, J. C. Soric, G. Moreno, and A. Alù, "Experimental verification of three-dimensional plasmonic cloaking in free-space," *New J. Phys.* **14**(1), 013054 (2012).
13. B. Orazbayev, N. Mohammadi Estakhri, M. Beruete, and A. Alù, "Terahertz carpet cloak based on a ring resonator metasurface," *Phys. Rev. B* **91**(19), 195444 (2015).

14. B. Zhu, G. Ren, S. Zheng, Z. Lin, and S. Jian, "Nanoscale dielectric-graphene-dielectric tunable infrared waveguide with ultrahigh refractive indices," *Opt. Express* **21**(14), 17089–17096 (2013).
15. I. V. Iorsh, I. S. Mukhin, I. V. Shadrivov, P. Belov, and Y. S. Kivshar, "Hyperbolic metamaterials based on multilayer graphene structures," *Phys. Rev. B* **87**(7), 075416 (2013).
16. T. Chen and S. He, "Frequency-tunable circular polarization beam splitter using a graphene-dielectric sub-wavelength film," *Opt. Express* **22**(16), 19748–19757 (2014).
17. I. Khromova, A. Andryieuski, and A. Lavrinenko, "Ultrasensitive terahertz/infrared waveguide modulators based on multilayer graphene metamaterials," *Laser Photonics Rev.* **8**(6), 916–923 (2014).
18. R. Z. Zhang and Z. M. Zhang, "Tunable positive and negative refraction of infrared radiation in graphene-dielectric multilayers," *Appl. Phys. Lett.* **107**(19), 191112 (2015).
19. J. S. Gomez-Diaz, C. Moldovan, S. Capdevila, J. Romeu, L. S. Bernard, A. Magrez, A. M. Ionescu, and J. Perruisseau-Carrier, "Self-biased reconfigurable graphene stacks for terahertz plasmonics," *Nat. Commun.* **6**, 6334 (2015).
20. A. Andryieuski, A. V. Lavrinenko, and D. N. Chigrin, "Graphene hyperlens for terahertz radiation," *Phys. Rev. B* **86**(12), 121108 (2012).
21. C. García-Meca, M. M. Tung, J. V. Galán, R. Ortuño, F. J. Rodríguez-Fortuño, J. Martí, and A. Martínez, "Squeezing and expanding light without reflections via transformation optics," *Opt. Express* **19**(4), 3562–3575 (2011).
22. M. Tamagnone, J. S. Gómez-Díaz, J. R. Mosig, and J. Perruisseau-Carrier, "Reconfigurable terahertz plasmonic antenna concept using a graphene stack," *Appl. Phys. Lett.* **101**(21), 214102 (2012).
23. P.-Y. Chen, M. Farhat, A. N. Askarpour, M. Tymchenko, and A. Alù, "Infrared beam-steering using acoustically modulated surface plasmons over a graphene monolayer," *J. Opt.* **16**(9), 094008 (2014).
24. J. S. Gómez-Díaz, M. Esquiús-Morote, and J. Perruisseau-Carrier, "Plane wave excitation-detection of non-resonant plasmons along finite-width graphene strips," *Opt. Express* **21**(21), 24856–24872 (2013).
25. M. Esquiús-Morote, J. S. Gomez-Diaz, and J. Perruisseau-Carrier, "Sinusoidally modulated graphene leaky-wave antenna for electronic beamscanning at THz," *IEEE Trans. Terahertz Sci. Technol.* **4**(1), 116–122 (2014).
26. Q. Sun, Y. Rostovtsev, and M. Zubairy, "Optical beam steering based on electromagnetically induced transparency," *Phys. Rev. A* **74**(3), 033819 (2006).
27. T. P. Steinbusch, H. K. Tyagi, M. C. Schaafsma, G. Georgiou, and J. Gómez Rivas, "Active terahertz beam steering by photo-generated graded index gratings in thin semiconductor films," *Opt. Express* **22**(22), 26559–26571 (2014).
28. C. T. DeRose, R. D. Kekatpure, D. C. Trotter, A. Starbuck, J. R. Wendt, A. Yaacobi, M. R. Watts, U. Chettiar, N. Engheta, and P. S. Davids, "Electronically controlled optical beam-steering by an active phased array of metallic nanoantennas," *Opt. Express* **21**(4), 5198–5208 (2013).
29. D. Kwong, A. Hosseini, Y. Zhang, and R. T. Chen, "1×12 Unequally spaced waveguide array for actively tuned optical phased array on a silicon nanomembrane," *Appl. Phys. Lett.* **99**(5), 051104 (2011).
30. K. Van Acoleyen, H. Rogier, and R. Baets, "Two-dimensional optical phased array antenna on silicon-on-insulator," *Opt. Express* **18**(13), 13655–13660 (2010).
31. S. H. Lee, J. Choi, H.-D. Kim, H. Choi, and B. Min, "Ultrafast refractive index control of a terahertz graphene metamaterial," *Sci. Rep.* **3**, 2135 (2013).
32. J. Cong, Y. Chen, J. Luo, and X. Liu, "Fabrication of graphene/polyaniline composite multilayer films by electrostatic layer-by-layer assembly," *J. Solid State Chem.* **218**, 171–177 (2014).
33. X. Liu, N. Wen, X. Wang, and Y. Zheng, "Layer-by-layer self-assembled graphene multilayer films via covalent bonds for supercapacitor electrodes," *Nanomater. Nanotechnol.* **5**, 1–7 (2015).
34. D. Qiu and E. K. Kim, "Electrically tunable and negative Schottky barriers in multi-layered graphene/MoS<sub>2</sub> heterostructured transistors," *Sci. Rep.* **5**, 13743 (2015).
35. B. Wunsch, T. Stauber, F. Sols, and F. Guinea, "Dynamical polarization of graphene at finite doping," *New J. Phys.* **8**(12), 318 (2006).
36. K. I. Bolotin, K. J. Sikes, Z. Jiang, M. Klima, G. Fudenberg, J. Hone, P. Kim, and H. L. Stormer, "Ultrahigh electron mobility in suspended graphene," *Solid State Commun.* **146**(9-10), 351–355 (2008).
37. D. A. Boyd, W.-H. Lin, C.-C. Hsu, M. L. Teague, C.-C. Chen, Y.-Y. Lo, W.-Y. Chan, W.-B. Su, T.-C. Cheng, C.-S. Chang, C.-I. Wu, and N.-C. Yeh, "Single-step deposition of high-mobility graphene at reduced temperatures," *Nat. Commun.* **6**, 6620 (2015).
38. L. Banszerus, M. Schmitz, S. Engels, J. Dauber, M. Oellers, F. Haupt, K. Watanabe, T. Taniguchi, B. Beschoten, and C. Stampfer, "Ultrahigh-mobility graphene devices from chemical vapor deposition on reusable copper," *Sci. Adv.* **1**(6), e1500222 (2015).
39. M. A. K. Othman, C. Guclu, and F. Capolino, "Graphene-dielectric composite metamaterials: evolution from elliptic to hyperbolic wavevector dispersion and the transverse epsilon-near-zero condition," *J. Nanophotonics* **7**(1), 073089 (2013).
40. S. A. Maier, *Plasmonics: Fundamentals and Applications* (Springer US, 2007).
41. M. A. K. Othman, C. Guclu, and F. Capolino, "Graphene-based tunable hyperbolic metamaterials and enhanced near-field absorption," *Opt. Express* **21**(6), 7614–7632 (2013).
42. M. Wakaki, T. Shibuya, and K. Kudodeceased, *Physical Properties and Data of Optical Materials* (CRC, 2007).
43. J. Neu, R. Beigang, and M. Rahm, "Metamaterial-based gradient index beam steerers for terahertz radiation," *Appl. Phys. Lett.* **103**(4), 041109 (2013).

44. I. V. Minin and O. Minin, *Diffractional Optics of Millimetre Waves* (CRC, 2004).
45. V. Pacheco-Peña, V. Torres, B. Orazbayev, M. Beruete, M. Navarro-Cía, M. Sorolla Ayza, and N. Engheta, "Mechanical 144 GHz beam steering with all-metallic epsilon-near-zero lens antenna," *Appl. Phys. Lett.* **105**(24), 243503 (2014).
46. B. E. A. Saleh and M. C. Teich, *Fundamentals of Photonics*, Wiley Series in Pure and Applied Optics (John Wiley & Sons, Inc., 1991).
47. V. Pacheco-Peña, V. Torres, M. Beruete, M. Navarro-Cía, and N. Engheta, " $\epsilon$ -near-zero (ENZ) graded index quasi-optical devices: steering and splitting millimeter waves," *J. Opt.* **16**(9), 094009 (2014).
48. S. Roberts, "Optical properties of copper," *Phys. Rev.* **118**(6), 1509–1518 (1960).
49. X. Chen, T. M. Grzegorzczak, B.-I. Wu, J. Pacheco, Jr., and J. A. Kong, "Robust method to retrieve the constitutive effective parameters of metamaterials," *Phys. Rev. E Stat. Nonlin. Soft Matter Phys.* **70**(1), 016608 (2004).
50. H. D. Hristov, *Fresnel Zones in Wireless Links, Zone Plate Lenses and Antennas* (Artech House, 2000).
51. H. Kogelnik, "Theory of dielectric waveguides," in *Integrated Optics, Topics in Applied Physics* (Springer, 1975), Vol. 7.
52. Z. Fei, A. S. Rodin, G. O. Andreev, W. Bao, A. S. McLeod, M. Wagner, L. M. Zhang, Z. Zhao, M. Thiemens, G. Dominguez, M. M. Fogler, A. H. Castro Neto, C. N. Lau, F. Keilmann, and D. N. Basov, "Gate-tuning of graphene plasmons revealed by infrared nano-imaging," *Nature* **487**(7405), 82–85 (2012).
53. J. Chen, M. Badioli, P. Alonso-González, S. Thongrattanasiri, F. Huth, J. Osmond, M. Spasenović, A. Centeno, A. Pesquera, P. Godignon, A. Z. Elorza, N. Camara, F. J. García de Abajo, R. Hillenbrand, and F. H. L. Koppens, "Optical nano-imaging of gate-tunable graphene plasmons," *Nature* **487**(7405), 77–81 (2012).
54. L. Yang, C. Pei, A. Shen, C. Zhao, Y. Li, X. Li, H. Yu, Y. Li, X. Jiang, and J. Yang, "An all-optical modulation method in sub-micron scale," *Sci. Rep.* **5**, 9206 (2015).

## 1. Introduction

Full control of electromagnetic waves, such as beam steering or shaping, is one of the most important challenges in applied electromagnetics. With the discovery of graphene, a one-atom-thick sheet of carbon, new roads for designing fast tunable electromagnetic devices have been opened [1–3]. By electrically or optically changing the Fermi level of graphene it is possible to modify its surface conductivity, which has applications in transformation optics [4], photonic integrated systems [5,6] or optical signal processing [7–9]. Thanks to its ultrathin nature, it can be incorporated into other materials on a subwavelength scale opening the door to metamaterials with exotic and tunable values of permittivity and permeability. These metamaterials can be advantageously used for the synthesis of ultra-compact devices operating in the THz regime, for a variety of applications such as super resolution imaging, cloaking, etc., overcoming the performance achievable with conventional, naturally available dielectrics [10–13].

Multilayer graphene-dielectric metamaterials have recently attracted the interest of the scientific community [14–18]. They consist of graphene sheets alternating with layers of a host dielectric [see inset in Fig. 1(a)]. In this configuration, the effective permittivity of the resulting metamaterial can be tuned by changing the surface conductivity of the graphene layers (it can be done, for example, by optical excitation or electric bias voltage [19]). Also, since the distribution of the chemical potential of graphene layers in the metamaterial can be arbitrary, it is possible to tailor an inhomogeneous medium for active control of light, e.g. beam steering, focusing, squeezing based on transformation optics, etc [15,20,21]. Graphene-based beam steerers (BSs) [22–25] offer a much higher modulation speed as compared to conventional devices, whose design is based on mechanical systems with movable mirrors, thermo-optic and acousto-optic phase tuning [26–30]. This makes graphene-based BSs promising for future optical data processing [1,31], where high modulation speed is required.

Leaky-wave antennas based graphene mono-layers [22–25] are feasible with the state-of-the-art technology and demonstrate good steering capabilities. However, their dimensions are limited by the attenuation of surface plasmon polaritons in graphene. BSs with multilayer graphene-dielectric metamaterials allow for bigger lateral dimensions and for a more efficient, directive beam steering. The physical aperture of metamaterial-based BSs is defined by the number of the layers of graphene and, consequently, by the cost and complexity of the constituent metamaterial fabrication. Unlike the experimentally tested monolayer graphene

technology, devices based on graphene multilayer structures or graphene metamaterials are beyond current fabrication capabilities and, for the moment, exist only as theoretical concepts. Nevertheless, recent advances in the fabrication and practical applications of multilayer graphene structures [32–34] can reduce the cost and complexity of the graphene metamaterial technology in the future.

In this paper, we propose a concept of a reconfigurable BS based on a multilayer graphene-dielectric metamaterial using three different approaches: (BS1) a GRIN metamaterial block, where the tunability of the graphene metamaterial is used to synthesize a prescribed phase change as a wave propagates through the structure; (BS2) a BS exploiting decoupled transmission channels (metallic parallel-plate waveguides filled with graphene-dielectric metamaterial) to create a phased array with high speed reconfiguration of each channel, enabling beam steering capability; and (BS3) a device that combines the previous designs by synthesizing an array of planar dielectric waveguides (transmission channels) in a graphene-dielectric metamaterial by defining a specific distribution of Fermi energy levels in graphene layers. The performance of all designs is investigated numerically, demonstrating their steering capability for a wide range of output angles. The results are compared against analytical calculations based on the Huygens-Fresnel principle.

The paper is organized as follows: in Section 2 we describe the properties of multilayer graphene-dielectric metamaterial and numerical methods used to simulate its infrared response. In Section 3 we define our proposed designs and illustrate the numerical results for each of them. Finally, in Section 4 we summarize the main results of our work.

## 2. Multilayer graphene-dielectric metamaterial

### 2.1 Graphene's conductivity

Graphene's conductivity  $\sigma_s$  can be modelled using the general Kubo formula [35]. In this work, it is calculated at ambient temperature  $T = 300$  K and scattering rate of  $\gamma = 10^{12} \text{ s}^{-1}$ , which corresponds to the experimentally measured mobility of exfoliated suspended graphene [36]. This is a relatively high value which is chosen as a best case, since our aim is to provide a clear principle demonstration. Lower quality graphene, fabricated using chemical vapor deposition (CVD), can worsen the performance of the proposed BSs. Nevertheless, constant improvements in graphene fabrication allow us to be optimistic and believe that high mobility may soon be reached in CVD samples, see [37,38]. Here and in the rest of this work we set the operating frequency at  $f = 20$  THz. For the chosen parameters, the calculated conductivity of graphene as a function of its chemical potential  $\mu$  is shown in Fig. 1(a).

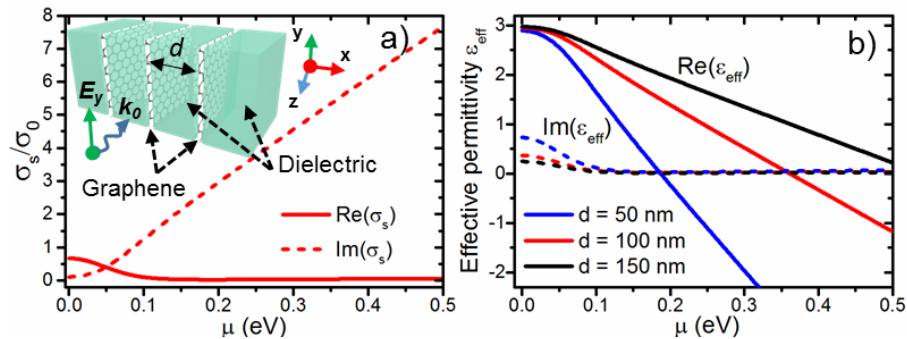


Fig. 1. (a) Graphene complex conductivity normalized to  $\sigma_0 = e^2/4\hbar = 0.061$  mS for  $T = 300$  K,  $\gamma = 10^{12} \text{ s}^{-1}$  at  $f = 20$  THz. (Inset) Geometry of the graphene-dielectric metamaterial. (b) Complex effective permittivity,  $\epsilon_{\text{eff}}$ , for  $\epsilon_m = 3$ ,  $T = 300$  K,  $f = 20$  THz and different values of spacer thickness  $d$ . Solid and dashed lines stand for real and imaginary parts, respectively.

## 2.2 Modelling a graphene-dielectric metamaterial

The graphene-dielectric metamaterial used in this work, consists of an array of graphene layers with period  $d$  and embedded in a host dielectric with permittivity  $\epsilon_m$  [17,39]. The structure is shown in the inset of Fig. 1(a). Its local permittivity can be tuned by changing the conductivity of graphene sheets. This can be done, for instance, by applying a bias voltage to each pair of the latter [17,19]. In this geometry, the electric field components parallel to graphene layers ( $E_y$ ,  $E_z$ ) see a metamaterial effective permittivity  $\epsilon_{eff}$ , whereas the perpendicular component ( $E_x$ ) sees the host dielectric permittivity  $\epsilon_m$ . Thus, the metamaterial permittivity tensor is:

$$\boldsymbol{\epsilon} = \begin{pmatrix} \epsilon_m & 0 & 0 \\ 0 & \epsilon_{eff} & 0 \\ 0 & 0 & \epsilon_{eff} \end{pmatrix} \quad (1)$$

where  $\epsilon_{eff}$  is the relative effective permittivity described by the following expression [40,41]:

$$\epsilon_{eff}(\omega, \mu, d) = \epsilon_m + \frac{i\sigma_s(\omega, \mu)}{d\omega\epsilon_0} \quad (2)$$

where  $d$  is the thickness of the host dielectric,  $\sigma_s$  is the graphene surface conductivity,  $\epsilon_0$  is the free space permittivity and  $\omega$  is the angular frequency. Cesium iodide (CsI,  $\epsilon_m = 3$ ) is chosen as a host dielectric since it has a good performance in terms of transparency and absorption losses in the infrared range [42]. The effective permittivity calculated as a function of the chemical potential  $\mu$  and different values of the spacer  $d$  is shown in Fig. 1(b). For small values of  $d$ , the curve for  $\text{Re}(\epsilon_{eff})$  is steeper, so that it can be tuned with small changes of graphene's Fermi energy. However, a small  $d$  increases  $\text{Im}(\epsilon_{eff})$  [see Fig. 1(b)] as well as the total number of graphene layers, raising losses in the metamaterial, as well as the cost and complexity of fabrication. As a compromise, a period  $d = 100$  nm is chosen, providing a broad tunability range ( $0.1 < \text{Re}(\epsilon_{eff}) < 2.8$ ) for relatively low values and range of graphene's chemical potential ( $350 \text{ meV} > \mu > 50 \text{ meV}$ ) and corresponding low values of the imaginary effective permittivity component ( $0.02 < \text{Im}(\epsilon_{eff}) < 0.2$ ).

Numerical simulations were performed using the frequency domain solver of COMSOL Multiphysics<sup>TM</sup>. The graphene-dielectric metamaterial was modelled using infinitesimally thin conductive layers for graphene sheets. Their dispersion was set using the Kubo formula. A fine hexahedral mesh was used with minimum and maximum mesh cell sizes of  $0.75 \mu\text{m}$  ( $0.05\lambda_0$ ) and  $1.5 \mu\text{m}$  ( $0.1\lambda_0$ ), respectively. A waveguide port with a vertically polarized electric field ( $E_y$ ) mode, impinging normally on the BS was used as a source. To reduce the computation time, all simulations were performed in a 2D geometry, imposing periodic boundary conditions along the  $y$ -axis. Perfectly matched layers were used for the rest of the boundaries to emulate open space.

## 3. Beam steerer based on graphene metamaterial

### 3.1 Graphene-dielectric metamaterial block (BS1)

The first design, BS1, is based on a phase delay line, created in a GRIN structure [43]. A linear distribution of the local refractive index in a medium steers the beam in the required direction. The scheme of the proposed BS1 is shown in Fig. 2(a). The GRIN medium is achieved by creating a spatial distribution of chemical potential values  $\mu(x)$  on the graphene-dielectric metamaterial.

Since the imaginary part of effective permittivity is small (see Sect.2.2) it is omitted in the analytical calculations for simplicity. Therefore the distribution of the refractive index  $n(x)$  of

the metamaterial along the  $x$ -axis, required for achieving a beam steering angle  $\theta$ , can be calculated using the ray tracing method, as follows [44,45]:

$$n(x) = \frac{\sin(\theta)}{L_z}(x - L_x) + n_{\max} \quad (3)$$

where  $x$  is the coordinate along the  $x$ -axis,  $n_{\max}$  is the maximum refractive index of the BS,  $L_x$  is the total width and  $L_z$  is the length of the BS1. The minimal length  $L_{z(\min)}$  depends on the maximum output angle and can be calculated as:

$$L_{z(\min)} = \frac{L_x \sin(\theta_{\max})}{\sqrt{\epsilon_{\max}} - \sqrt{\epsilon_{\min}}} \quad (4)$$

where  $\theta_{\max}$  is maximum output angle, and  $\epsilon_{\max}$ ,  $\epsilon_{\min}$  are the extreme values of the real permittivity attainable in the considered graphene-dielectric metamaterial.

Since the material is a GRIN medium, the beam inside the structure is focused towards the side with a higher refractive index [46]. For high values of  $\theta$ , the gradient of the refractive index becomes steeper, which results in a focusing of the transmitted beam (as it will be shown later). In the limit, this can even cause a reflection back to the input. To obtain the maximum achievable angle,  $\theta_{\text{theor}}$ , we analyse light propagation inside a GRIN medium using the Eikonal equation under the formalism of ray theory [46]:

$$\frac{d^2x}{dz^2} = \frac{1}{n(x)} \frac{dn(x)}{dx} \quad (5)$$

By inserting Eq. (3) into Eq. (5) and after solving the differential equation we obtain the ray trajectory  $x(z)$  [46] [see dashed line in Figs. 3(a)-3(c)]. The output angle  $\theta'$  of the ray can be derived using the slope of the trajectory at the output  $\theta_{sl} = dx/dz$  particulated at  $(x = x_{out}, z = L_z)$  and Snell's law:  $\theta' = \sin^{-1}[n(x_{out})\sin(\theta_{sl})]$ , where  $n(x_{out})$  is the refractive index at the output  $(x = x_{out})$ . Note, that since the ray theory allows finding the actual ray slope at the output surface, the final output angle  $\theta'$  can slightly deviate from the design output angle  $\theta$ , which is derived using approximate equations, without taking into account ray propagation inside the GRIN medium.

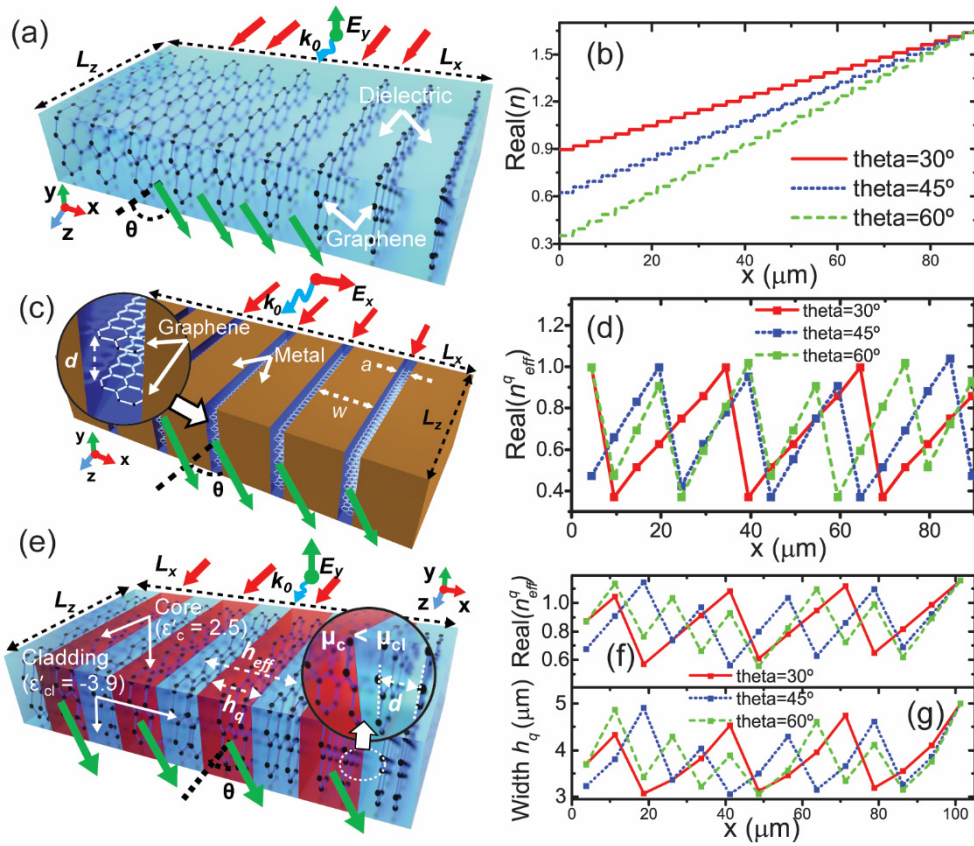


Fig. 2. Schemes for the BS1 (a), BS2 (c) and BS3 (e). (b), (d), (f) Real part of the effective refractive index vs the  $x$  coordinate for the BS1, BS2, and BS3, respectively. (g) Spatial distribution of the widths  $h_q$  in BS3.

Since the beam is refracted towards the side with higher refractive index, an analogy between a GRIN lens and the proposed GRIN BS (BS1) can be drawn. The focal length  $FL$  (distance from the output surface of the BS1 to the focal point) can be calculated as  $FL = (L_x - x_{out})/\tan(\theta')$  (in this case we define the optical axis at  $x = L_x$ ). Therefore, by numerically solving Eq. (5) and extracting the focal distance as a function of the design output angle  $\theta$ , the maximum output angle  $\theta_{theor} = 66^\circ$  is found, which corresponds to the case when the beam is focused exactly at the output surface ( $FL = 0$ ). In order to minimize the length  $L_z$  of the BS and therefore losses, in this work  $\theta_{max} = 60^\circ$  (with  $\epsilon_{max} = 2.7$ ,  $\epsilon_{min} = 0.1$  and corresponding  $\mu_{min} = 0.06\text{eV}$ ,  $\mu_{max} = 0.35\text{ eV}$ ,  $L_z = 58\ \mu\text{m}$ ) is chosen, slightly smaller than the theoretical maximum angle  $\theta_{theor}$ .



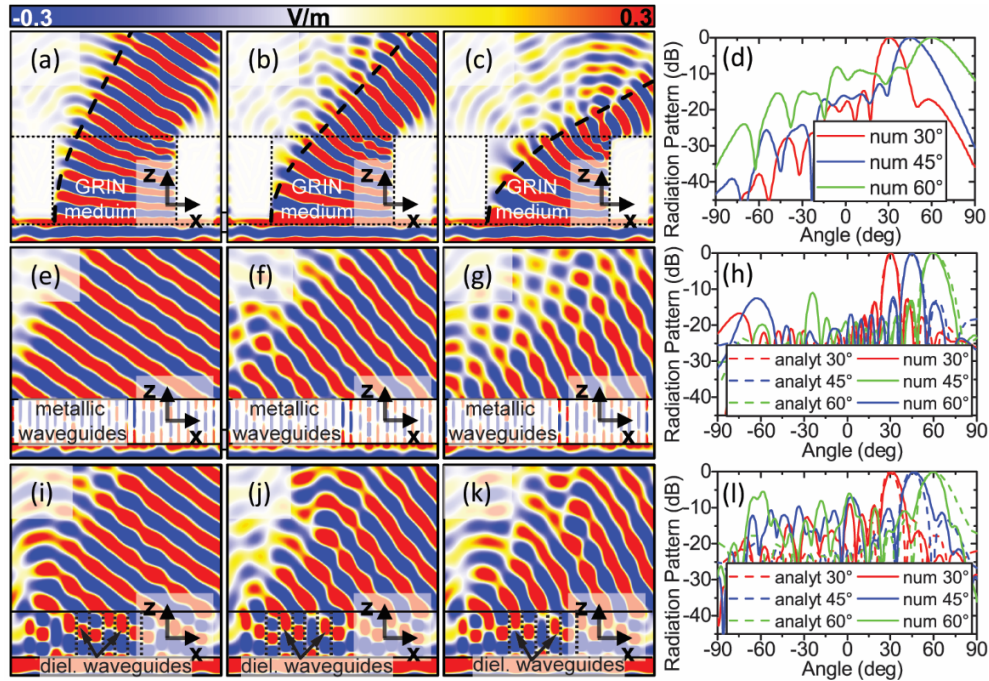


Fig. 3. Numerically calculated magnitude of the  $E_y$ -field for the first (a-c), second (e-g) and third design (i-k) for output angles:  $\theta = 30^\circ$  (first column, a,e,i),  $\theta = 45^\circ$  (second column, b,f,j),  $\theta = 60^\circ$  (third column, c,g,k). Black dashed lines in (a-c) represent the analytical solutions for the ray propagation inside the GRIN medium. (d), (h) and (l) show the radiation patterns of the BS1, BS2, and BS3, respectively, analytically (dashed) and numerically (solid) calculated for the output angles of  $30^\circ$  (red),  $45^\circ$  (blue), and  $60^\circ$  (green).

Once the effective refractive index profile is obtained, the corresponding values of the chemical potential  $\mu(x)$  of graphene layers can be interpolated using (1). To simplify the structure, the required ideally smooth spatial distribution of the metamaterial effective index of refraction is discretized in 30 steps [see Fig. 2(b)]. The final design of the BS1 is shown in Fig. 2(a) and has the following dimensions:  $L_x = 6\lambda_0 = 90 \mu\text{m}$ ,  $L_z = 3.8\lambda_0 = 58 \mu\text{m}$ . The total number of graphene layers is  $N = L_x/d = 900$ . The tunability of the BS1 is numerically checked by means of full-wave simulations, performed in COMSOL Multiphysics<sup>TM</sup>. The output angles are obtained as a function of the inclination of the chemical potential  $inc = \Delta\mu/\Delta x$  in the BS1's profile, where  $\Delta\mu$  is the change of chemical potential induced by the gating voltage difference and  $\Delta x$  is the variation of the coordinate  $x$ . The result is plotted in the Fig. 4 (solid red line). The maximum output angle for the specified parameters is  $\theta_{\max}^{(1)} = 63^\circ$ . Larger angles are impossible to achieve due to the reflection of the incident wave inside the structure. This is in good agreement with the previously calculated theoretical maximum angle  $\theta_{\text{theor}}$ .



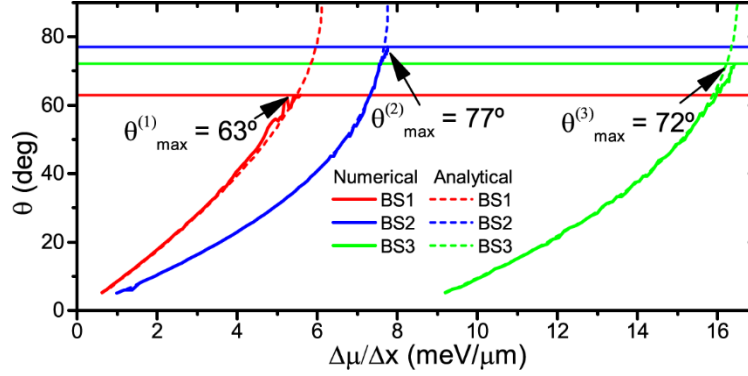


Fig. 4. Analytically (dashed lines) and numerically (solid lines) calculated output angles of the BSs vs the inclination of the graphene's chemical potential  $\Delta\mu/\Delta x$  in the metamaterial for the BS1 (red), BS2 (blue) and BS3 (green). Horizontal solid lines represent the maximum output angles for the three BS designs.

For illustrative purposes, the performance of all three designed BSs is analyzed at 3 different output angles:  $30^\circ$ ,  $45^\circ$  and  $60^\circ$ . The  $E_y$ -field magnitude distribution obtained for these angles for the BS1 is presented in Figs. 3(a)-3(c). As can be seen from Fig. 3(c), due to the steep profile of the refractive index the beam is focused at the output. This leads to a significantly reduced effective aperture of the BS1, which broadens the beamwidth. For extreme angles ( $\theta > 50^\circ$ ), this provokes higher side lobes due to reflection at the BS1 borders. This is demonstrated in Fig. 3(d), where one can see that the side lobe level for  $\theta = 60^\circ$  is higher than for  $\theta = 30^\circ$ ,  $45^\circ$ . The radiation properties of all three analyzed BSs are summarized in Table 1.

### 3.2 Array of parallel-plate metallic waveguides filled with graphene-dielectric metamaterial (BS2)

As it can be seen in Figs. 3(a)-3(c), the BS1 design is relatively simple and provides good performance for small output angles, but it has a fundamental limitation on the maximum output angle due to the ray refraction inside the GRIN medium. One way to overcome this limitation is to recall the phased array principle, where each phase delay line is isolated from the adjacent lines, providing a more uniform phase and amplitude distribution at the output [45,47]. This idea is exploited in the BS2 design we describe in this Section.

The BS2 consists of an array of metallic parallel-plate waveguides of identical height  $a$  (working at single mode regime), filled with graphene-dielectric metamaterial [17,28] [see sketch in Fig. 2(c)]. To obtain the required local phase delay at the output of such structure, we tune the effective refractive index  $n_{eff}$  of the  $q^{th}$  parallel-plate waveguide core, thus, changing the propagation constant  $\beta^q$  of its TEM mode:

$$\beta^q = k_0 n_{eff}^q \quad (6)$$

where  $k_0$  is the wave vector in free space and  $q$  is an integer denoting each waveguide. Here, analogously to the previous design, only the real part of refractive index is considered due to the small values of the imaginary part.

In order to reduce the length of the waveguides, and hence their weight and losses, the modulo of  $2\pi$  is applied to the output phase. The required phase at the output of the  $q^{th}$  waveguide and its length are calculated as follows [45,47]:

$$\phi^q = \beta^0 L_z - \text{mod}(k_0 x^q \sin(\theta), 2\pi) \quad (7)$$

$$L_z = \frac{2\pi}{\beta_{\max} - \beta_{\min}} \quad (8)$$

where  $\beta^0 = \beta_{\max}$  is the propagation constant of the guided mode in the reference waveguide,  $q = 1, 2, 3 \dots$  is the number of waveguide,  $\theta$  is the output angle,  $x^q$  is the  $x$  coordinate of the  $q^{\text{th}}$  waveguide,  $L_z$  is the length of the waveguides,  $\beta_{\max} = k_0 n_{\text{eff}}^{(\max)}$  and  $\beta_{\min} = k_0 n_{\text{eff}}^{(\min)}$  are maximal and minimal propagation constants respectively [ $n_{\text{eff}}^{(\max)}$ ,  $n_{\text{eff}}^{(\min)}$  are maximal and minimal effective refractive indices of the waveguide core, which are chosen to provide high and uniform transmission coefficient  $S_{21}(n_{\text{eff}})$  for all values of refractive index ( $n_{\text{eff}}^{(\min)} \leq n_{\text{eff}} \leq n_{\text{eff}}^{(\max)}$ )]. Finally, the effective refractive index  $n_{\text{eff}}^q$  of the  $q^{\text{th}}$  waveguide core required to obtain a desired output phase delay  $\phi^q$  can be defined as:

$$n_{\text{eff}}^q = \frac{\phi^q}{k_0 L_z} \quad (9)$$

The distribution of  $n_{\text{eff}}^q$  is shown in Fig. 2(d). The corresponding values of the chemical potential  $\mu^q$  of graphene layers in the  $q^{\text{th}}$  waveguide can be interpolated using Eq. (3). The final BS design consists of a total  $q = 25$  waveguides with height  $a = 1 \mu\text{m}$ , separated by metallic walls with thickness  $w = 4 \mu\text{m}$ , which gives a total period of  $p = 5 \mu\text{m}$  [see Fig. 2(c)]. From additional simulations for one waveguide  $n_{\text{eff}}^{(\max)} = 1.05$  and  $n_{\text{eff}}^{(\min)} = 0.32$  are found, which provide a flat response of  $S_{21}(n_{\text{eff}}) > -2\text{dB}$ . Thus the final dimensions are: total width  $L_x = 25p = 125 \mu\text{m}$  ( $8.3\lambda_0$ ), and length  $L_z = 20.5 \mu\text{m}$  ( $1\lambda_0$ ).

Unlike the BS1, the BS2 structure is excited with a horizontally polarized ( $E_x$ ) waveguide port in order to excite the TEM mode in each waveguide [Fig. 2(c)]. The rest of the boundaries remain unchanged. In our numerical model, the metallic walls are made of copper. At the design frequency  $f = 20 \text{ THz}$ , the analytical skin depth in the copper is  $\delta_{\text{Cu}} = 0.03 \mu\text{m}$  [48], which is much smaller than the thickness of the walls. To reduce the computation time, we use the tensorial effective medium approximation for the graphene-dielectric metamaterial, Eqs. (1) and (2). To prove the validity of this approach we simulate a single waveguide filled with homogeneous dielectric and graphene-metamaterial. The refractive index of the effective medium can be extracted from the scattering parameters  $S_{11}$  and  $S_{21}$ , using a retrieval method [49]. Figure 5 shows the refractive indices extracted from the  $S$ -parameters for the waveguide filled with graphene-dielectric metamaterial and an equivalent homogeneous dielectric. As it can be seen, the retrieved refractive indices perfectly match the analytical values, confirming the validity of the metamaterial homogenization.

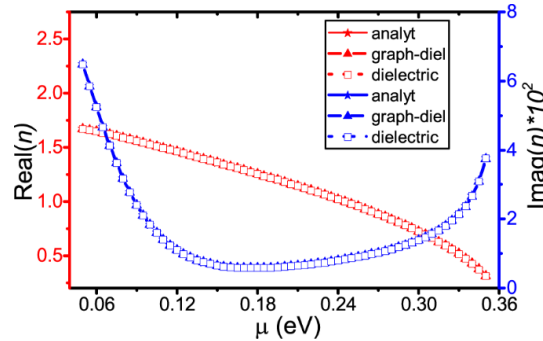


Fig. 5. Analytically (solid lines) and numerically calculated effective refractive index for a TEM mode of a parallel-plate waveguide filled with a dielectric medium (dotted lines) and with graphene-dielectric metamaterial (dashed lines). This shows the validity of tensorial effective medium approach for BS2 for faster calculations.

Analogously to the BS1, the steering capability of BS2 is studied using full-wave simulations. The output angle is tuned by changing the inclination of the chemical potential in the metamaterial  $inc = \Delta\mu/\Delta x$ . The numerically obtained output angles for the second BS design are shown in Fig. 4 (solid blue line). The maximum angle is  $\theta_{\max}^{(2)} = 77^\circ$ , which is larger than in the previous design. However, the designed maximum angle  $90^\circ$  (dashed blue line) is never reached, which can be explained by the non-isotropic radiation pattern of each phased array element (end of each waveguide). Therefore, an array of such elements cannot reach end-fire performance.

The numerically obtained  $E_x$ -field distributions in the  $xz$ -plane for the BS2 are shown in Figs. 3(e)-3(g). The results demonstrate that the structure can bend the plane wave incident at  $0^\circ$  to output angles of  $30^\circ$ ,  $45^\circ$  and  $60^\circ$ . Moreover, it can be seen that the wavefronts at the output for all angles are closer to a plane wavefront than the ones observed in BS1, Figs. 3(a)-3(c). This can be explained by a more uniform distribution of the amplitudes and phases at the output, since the beam in the BS2 is not focused at the output, thanks to decoupled transmission channels. The numerically obtained radiation patterns of the BS2 are plotted for the three angles considered in Fig. 3(h) and compared with analytical results, obtained with the Huygens-Fresnel method considering an array of isotropic sources with same amplitude (which has not been applied in the first design due to a more complicated amplitude and phase distribution at the output of the BS1) [44,50]. The analytical and simulated radiation patterns are almost identical for all angles and coincide with the design output angles. However, from Fig. 3(h), it is also clear that the grating lobes increase for large output angles due to the finite period  $p$  of the waveguide array. As shown in Table 1, the reflection coefficient  $\Gamma$  of the BS2 is below  $-5.2$  dB in all cases. As expected, it is significantly higher than for the BS1, due to the higher impedance mismatch between free space and the array of metallic waveguides.

### 3.3 Array of planar waveguides made entirely of graphene metamaterial (BS3)

The array of metallic waveguides provides better performance in terms of beamwidth and maximum output angle. However, the BS2 requires complex fabrication due to the small distance between waveguides,  $w$ . It is possible to increase the period  $p$  of the array at the cost of higher grating lobes. However, thicker metallic walls also increase the impedance mismatch of the BS2 with free space, resulting in a higher reflection loss of the device.

These limitations are overcome in the BS3 design, which is a combination of the previous concepts of BS1 and BS2 and consists of a phased array of planar waveguides, created in the graphene-dielectric metamaterial by alternating the regions (waveguide core and cladding) with high contrast of refractive indices ( $n_c \gg n_{cl}$ ). This can be obtained through non-uniform doping of graphene layers in the metamaterial, resulting in a totally reconfigurable system.

The propagation constant  $k_0 n_{eff}^q$  of the mode  $m$  in each waveguide  $q$  can be found using the dispersion equation of a planar waveguide [51]:

$$h_q k_0 \sqrt{\epsilon'_c - (n_{eff}^q)^2} = 2 \tan^{-1} \left( \frac{\sqrt{(n_{eff}^q)^2 - \epsilon'_{cl}}}{\sqrt{\epsilon'_c - (n_{eff}^q)^2}} \right) + \pi(m-1) \quad (10)$$

where  $h_q$  is the waveguide width,  $k_0$  is the wave vector in free-space,  $\epsilon'_c$ ,  $\epsilon'_{cl}$  are the real values of the effective permittivity of the core and cladding respectively,  $n_{eff}^q$  is the effective refractive index of the mode in each  $q$  waveguide, and  $m = 1, 2, 3, \dots$  is the mode number. For the sake of simplicity and in order to minimize the width  $h_q$ , a single-mode waveguide configuration is chosen ( $m = 1$ ).

The length of each waveguide and the output phase at its end are calculated using Eqs. (7) and (8), similarly to the previous designs considering only the real part of the effective index of refraction. To minimize mutual coupling between adjacent waveguides, a certain minimal

distance between them is required. This increases the period of the array and therefore can lead to higher grating lobes. To reduce the effective width of each waveguide or the distance between waveguides, it is necessary to minimize the mutual coupling effect or, in other words, provide strong guiding in each element. The effective width of the waveguides can be found as:  $h_{eff} = h_q + 2/[k_0(\epsilon'_c - \epsilon'_{cl})]$  [51]. Therefore, our aim is to increase the difference between the effective permittivity of the core  $\epsilon'_c$  and the cladding  $\epsilon'_{cl}$  so that the effective width  $h_{eff}$  is reduced.

In our particular case layers with real values of effective permittivity  $\epsilon'_c = \epsilon_{max} = 2.5$  ( $\epsilon''_c = 0.1$ ) and  $\epsilon'_{cl} = \epsilon_{min} = -3.9$  ( $\epsilon''_{cl} = 0.05$ ) are used which correspond to values of chemical potential  $\mu_{min} = 0.08$  eV and  $\mu_{max} = 0.82$  eV, respectively. The cladding with negative effective permittivity acts as a weakly metallic wall, which results in a smaller field penetration [18] into the cladding (analytical skin depth  $\delta_w = \lambda[2\pi(-\epsilon'_{cl})^{1/2}]^{-1} = 1.2$   $\mu\text{m}$ ) and therefore smaller period of waveguides,  $s$ . However, since at mid-infrared frequencies and for the considered doping levels, the real part of the conductivity of graphene layer is noticeably smaller than in metals (e.g. copper or silver) such “metallic” medium provides lower losses [14]. Thus, for the chosen values of permittivity the minimal period of waveguides  $s_{min} = 7.5$   $\mu\text{m}$  ( $>h_q$ ) is achieved. Analogously to the previous BS design, the modulo of  $2\pi$  is applied to the output phase in order to reduce the length of the waveguides and therefore the losses. Moreover, the shorter length of the waveguides also reduces the coupling between adjacent waveguides, which is proportional to their length.

From Eq. (10), the propagation constant (or effective refractive index) in each planar waveguide can be tuned by changing either the core permittivity or the width of the waveguide. However, a small core permittivity  $\epsilon'_c$  is not desired, since it increases the effective width of the core. Thus, the effective refractive index of each planar waveguide is tuned from  $n_{eff}^{(min)} = 0.52$  to  $n_{eff}^{(max)} = 1.56$  by varying the waveguide width from  $h_q = 3$   $\mu\text{m}$  to  $5$   $\mu\text{m}$ . After calculating the phase profile at the output, using Eq. (7), the corresponding effective refractive indices  $n_{eff}^q$  are obtained. The final distributions of  $n_{eff}^q$  for the chosen parameters are shown in Fig. 2(f). The corresponding values of the waveguide widths  $h_q$  can be found from Eq. (9) and they are shown in Fig. 2(g). The final geometry is similar to the first BS design shown in Fig. 2(a). It has the following dimensions:  $L_x = 14h_q = 105$   $\mu\text{m}$ ,  $L_z = 23.5$   $\mu\text{m}$  ( $1.2\lambda_0$ ) [Fig. 2(e)]. The total number of graphene layers is  $N = L_x/d = 1050$ .

The performance of the BS3 is evaluated by changing the inclination of the refractive index  $inc = \Delta\mu/\Delta x$ . The numerically obtained output angles of the BS3 are shown in Fig. 4 (solid green line) and compared with design pre-set values (dashed green line). Similar to the BS2, the beam steering angle of  $90^\circ$  is never reached. This is also due to the finite directivity of each phased array element, i.e. non-isotropic radiation of an open waveguide. Moreover, the maximum angle of the BS3 is  $\theta_{max}^{(3)} = 72^\circ$ , which is slightly smaller than in the BS2 design. This is due to the fact that the aperture of each waveguide in the array is larger than in the previous design ( $h_q > a$ ), resulting in a more directive radiation.

Finally, as for the previously discussed BS1 and BS2 designs, the performance of the BS3 is investigated at three demonstrative output angles:  $30^\circ$ ,  $45^\circ$  and  $60^\circ$ . The obtained  $E_y$ -field distributions in  $xz$ -plane are shown in Figs. 3(i)-3(k). There are some perturbations of the field, which can be related to the numerically obtained effective refractive indices  $n_{eff}^q$  slightly differing from their analytical values, and the mutual coupling between adjacent waveguides. The numerical and analytical  $E$ -field patterns are plotted in Fig. 3(l). The grating lobes in BS3 are higher than in the BS2. This can be explained by the larger period of the waveguide array,  $s = 7.5$   $\mu\text{m} \geq \lambda_0/2$ , and a less uniform distribution of the amplitude at the output due to the factors described above. The reflection coefficient  $\Gamma$  of the BS3 is below

-14 dB for all angles, which is much lower than in the BS2. This can be attributed to a better coupling between the incident field and waveguide modes due to bigger apertures of the waveguides ( $h_q$ ). To facilitate the comparison of the three BS designs, all numerical results are summarized in Table 1.

As mentioned in Sect. 2, all the calculations were done assuming low values of the scattering rate of the graphene ( $\gamma = 10^{12} \text{ s}^{-1}$ ). To demonstrate the impact of losses in graphene on the performance of the designed BSs, we ran additional simulations with higher scattering rate,  $\gamma = 10^{13} \text{ s}^{-1}$ . The corresponding numerical results are presented in Table 1 (values in the parentheses). Poorer quality of graphene deteriorates the performance in all BS designs, which is noticed in the increased side lobe and reflection levels.

An open question that remains to be answered is the practical realization of the structures we propose here. Fortunately, recent advances in the fabrication of multilayer graphene [32–34] let us be optimistic about the feasibility of such structures in the near future. Additionally, biasing multilayer graphene seems difficult in practice. One can use self-biased graphene layers [19] connected to opposite poles of a voltage source. Finally, if bias voltage should be avoided, graphene layers can be excited optically [52–54].

#### 4. Conclusion

In this work, we propose and numerically analyze three different designs of mid-infrared beam steering devices based on graphene-dielectric metamaterial: (1) GRIN graphene-based metamaterial block, (2) an array of metallic waveguides filled with graphene-dielectric metamaterial and (3) an array of planar waveguides created in a graphene-dielectric metamaterial block with a specific spatial profile of graphene sheets doping. All designs demonstrate an effective beam control over a wide range of output angles: from  $0^\circ$  to  $70^\circ$  for the considered metamaterial parameters. The numerical results are in a good agreement with analytical results based on Huygens Fresnel method. The calculated radiation patterns demonstrate low side lobe levels of  $-11.9 \text{ dB}$  for small output angles ( $\leq 30^\circ$ ). The BS1 provides good side lobe levels with low reflection losses, however it is limited by the maximum output angle. The BS2 along with the low side lobe levels and a more robust design has large range of output angles. As penalty the higher reflection losses are presented, reducing the overall efficiency. The BS3, phased array of the planar graphene-dielectric waveguides, which provides a totally reconfigurable mechanism of beam control, demonstrates an acceptable side lobe level, while maintaining a low reflection coefficient of  $-14 \text{ dB}$  for all sample output angles. Such graphene-dielectric metamaterial BSs are promising ultrafast electro-optical and all-optical tunable devices for imaging, sensing and communication applications, which require the small level of reflection losses.

**Table 1. Numerical Analysis of the Three Proposed BSs**

Steering angle $\theta$ , $^\circ$	Output angle, $^\circ$			$\Gamma^a$ , dB			HPBW <sup>b</sup> , $^\circ$			SLL <sup>c</sup> , dB		
	30	45	60	30	45	60	30	45	60	30	45	60
BS1 <sup>d</sup>	30.8 (29.3)	44.9 (43.4)	59.9 (-)	-7.8 (-6.8)	-8 (-6.8)	-8.1 (-6.9)	12.8 (13.7)	18.3 (21.9)	22.5 (-)	-14.7 (-10.1)	-12.9 (-5.5)	-8.1 (-)
BS2 <sup>e</sup>	30 (30)	45 (45)	60 (60)	-6.1 (-2.4)	-5.2 (-2.4)	-5.5 (-2.4)	6.8 (6)	8.4 (7.3)	11.4 (10.4)	-12.7 (-12.5)	-12.1 (-11.7)	-11 (-11.8)
BS3 <sup>f</sup>	30.8 (29.8)	46.4 (44.9)	59.4 (59.4)	-15.1 (-14.3)	-14.7 (-14)	-15.3 (-14.1)	8.4 (7.8)	10 (10)	13.8 (13.2)	-11.9 (-7.6)	-8.9 (-6.4)	-7.3 (-4.4)

<sup>a</sup> $\Gamma$  is the reflection coefficient.

<sup>b</sup>HPBW is the half-power beam width.

<sup>c</sup>SLL is the side-lobe level.

<sup>d</sup>BS based on metamaterial block.

<sup>e</sup>BS based on array of parallel plate waveguides.

<sup>f</sup>BS based on array of waveguides implemented in a graphene metamaterial block with no additional materials.

In the parentheses are given parameters for  $\gamma = 10^{13} \text{ s}^{-1}$ .

## **Acknowledgments**

This work was supported in part by the Spanish Government under Contract TEC2014-51902-C2-2-R and the Government of the Russian Federation [Grant No. 074-U01]. B. O. is sponsored by the Spanish Ministerio de Economía y Competitividad under grant FPI BES-2012-054909. M.B. is sponsored by the Spanish Government via RYC-2011-08221. I.K. is sponsored by the Russian Foundation for Basic Research under grant No. 14-07-31272.